AGU PUBLICATIONS

JGR

Journal of Geophysical Research: Oceans

RESEARCH ARTICLE

10.1002/2014JC010231

Structure of turbulence and sediment stratification in wave-supported mud layers

Abbas Hooshmand[1], Alexander R. Horner-Devine[1], and Michael P. Lamb[2]

[1]Department of Civil and Environmental Engineering, University of Washington, Seattle, Washington, USA, [2]Division of Geological and Planetary Sciences, California Institute of Technology, Pasadena, California, USA

Key Points:
- Ripples dominate near-bed dynamics in low-velocity conditions
- Density stratification suppresses turbulence in high-velocity conditions
- Suspension of sand controls the generation of high-concentration mud layers

Correspondence to:
A. R. Horner-Devine,
arhd@uw.edu

Citation:
Hooshmand, A., A. R. Horner-Devine, and M. P. Lamb (2015), Structure of turbulence and sediment stratification in wave-supported mud layers, *J. Geophys. Res. Oceans*, *120*, 2430–2448, doi:10.1002/2014JC010231.

Received 10 JUN 2014
Accepted 12 FEB 2015
Accepted article online 18 FEB 2015
Published online 2 APR 2015

Abstract We present results from laboratory experiments in a wave flume with and without a sediment bed to investigate the turbulent structure and sediment dynamics of wave-supported mud layers. The presence of sediment on the bed significantly alters the structure of the wave boundary layer relative to that observed in the absence of sediment, increasing the TKE by more than a factor of 3 at low wave orbital velocities and suppressing it at the highest velocities. The transition between the low and high-velocity regimes occurs when $Re_\Delta \simeq 450$, where Re_Δ is the Stokes Reynolds number. In the low-velocity regime ($Re_\Delta < 450$) the flow is significantly influenced by the formation of ripples, which enhances the TKE and Reynolds stress and increases the wave boundary layer thickness. In the high-velocity regime ($Re_\Delta > 450$) the ripples are significantly smaller, the near-bed sediment concentrations are significantly higher and density stratification due to sediment becomes important. In this regime the TKE and Reynolds stress are lower in the sediment bed runs than in comparable runs with no sediment. The regime transition at $Re_\Delta = 450$ appears to result from washout of the ripples and increased concentrations of fine sand suspended in the boundary layer, which increases the settling flux and the stratification near the bed. The increased stratification damps turbulence, especially near the top of the high-concentration layer, reducing the layer thickness. We anticipate that these effects will influence the transport capacity of wave-supported gravity currents on the continental shelf.

1. Introduction

Rivers carry large volumes of terrestrially derived sediments to the coast and discharge them onto the continental shelf [*Milliman and Meade*, 1983], where they are dispersed by shelf processes [*Nittrouer and Wright*, 1994; *Wheatcroft et al*., 2007]. These processes determine how sediment is redistributed on the shelf [*Wright et al*., 1997, 1999, 2001] and whether it is transported off the shelf into the abyssal ocean. This latter outcome is of particular importance because it represents a flux of sediment, carbon, and nutrients out of the shelf system into the abyssal ocean where it is no longer available to the coastal ecosystem.

Once they have been discharged into shelf waters, river-borne sediment may settle near the river mouth or further from the mouth [*Geyer et al*., 2000; *McPhee-Shaw et al*., 2007; *Walsh et al*., 2004]. The sediment deposition depends on the ratio of sediment to freshwater discharge [*Wright and Friedrichs*, 2006], flocculation [*Safak et al*., 2013], or other processes such as convective instabilities due to particle settling in the plume [*Parsons et al*., 2001] that affect their removal from the plume. Once they have been deposited on the shelf, they may be moved across the shelf as turbidity currents if the shelf is steep [*Hamblin and Walker*, 1979; *Ma et al*., 2008]. However, most shelves are not sufficiently steep to support seaward transport of sediment due to gravity alone [*Wright and Friedrichs*, 2006]. On gently sloping shelves, additional shear from shelf currents or surface waves is required to generate sufficient sediment suspension and maintain cross-shelf sediment transport. This study focuses solely on wave-generated suspensions.

Surface waves can generate significant bottom stresses on the shelf, though the stresses are strongest in shallower regions and only felt in deeper regions in storm conditions. When wave action and sediment supply are sufficient, this process generates thin $\mathcal{O}(10\,\mathrm{cm})$, high-concentration $\mathcal{O}(50\,\mathrm{g\,L^{-1}})$ sediment layers that move downslope across the shelf due to gravity and are referred to as Wave-Supported Gravity Currents (WSGC) [*Wright and Friedrichs*, 2006]. WSGCs have been observed on continental shelves near many river mouths, such as the Eel River [*Ogston et al*., 2000; *Traykovski et al*., 2000], Waiapu River [*Ma et al*., 2008],

Po River [*Traykovski et al*., 2007], Atchafalaya River [*Jaramillo et al*., 2009], and Waipaoa River [*Hale et al*., 2014]. WSGCs can transport sediment seaward until the shelf is so deep that the waves do not penetrate to the bottom and shear stress becomes small. At this point, the current may continue if the shelf is sufficiently steep, or it will die out and the sediment will be deposited [*Traykovski et al*., 2000; *Wright and Friedrichs*, 2006].

Wave-supported gravity currents are considered to be one of the primary mechanisms for cross-shelf sediment transport on continental shelves [*Wright and Friedrichs*, 2006]. Many field observations show the importance of these events (see previous paragraph) and a number of models have been developed based on available field data [*Wright et al*., 2001; *Scully et al*., 2002; *Traykovski et al*., 2007; *Falcini et al*., 2012]. However, field observations generally cannot resolve the structure of WSGCs in sufficient details to fully describe their dynamics or test model assumptions. Numerical modeling [e.g., *Colney et al*., 2008; *Ozdemir et al*., 2010a] and laboratory experiments [*Lamb et al*., 2004; *Lamb and Parsons*, 2005; *Liang et al*., 2007; *Yan et al*., 2010] that can resolve the structure of these currents may provide the information necessary to improve our ability to model the transport rates in WSGCs and the conditions necessary for their formation.

Here we present new laboratory experiments that investigate the generation and turbulent structure of high-density sediment suspensions over a flat bed similar to those observed on the continental shelf. The experiments use new instrumentation that resolves the temporal and vertical structure of the sediment and turbulent velocity fields in sufficient detail to determine the underlying physical relationships in WSGCs. The experiments and analysis focus explicitly on the competing influence of bed ripples and density stratification, in order to understand when these are important and the role they play in the dynamics of WSGCs.

2. Background

In the late 1990s, several field observations from the STRATAFORM program played a major role in improving our understanding of sediment transport across continental shelves [*Nittrouer*, 1999; *Ogston et al*., 2000; *Geyer et al*., 2000]. Observations from the Eel River margin emphasized the important role of surface waves in cross-shelf sediment flux and showed that a few significant storm events contributed most of the flux [*Ogston et al*., 2000; *Puig et al*., 2003]. *Traykovski et al*. [2000] examined the velocity and sediment concentration profiles during a number of wave-induced transport events, showing that fluid mud is trapped in a thin layer whose thickness is similar to the wave boundary layer. Although velocity measurements were not possible within the mud layer, they observed enhancement of the velocity 0.5 mab relative to 1 and 2 mab during at least one major wave resuspension event and concluded that this is evidence of downslope gravitational transport. Based on the expected wave penetration, bottom slope, and depth, they concluded that this mud layer loses energy and is deposited at a depth of 90–110 m. A series of models have been developed to predict the cross-shelf flux of sediment in WSGCs, primarily based on a linearized form of the Chezy equation [*Wright et al*., 2001; *Scully et al*., 2002; *Traykovski et al*., 2007]. *Wright et al*. [2001] and *Scully et al*. [2002] relate sediment concentration to wave stress assuming a critical value of the bulk Richardson number Ri_b of 0.25. However, estimates from prior laboratory experiments find that Ri_b is approximately an order of magnitude smaller than this assumed value [*Lamb et al*., 2004], motivating a clearer understanding of the underlying dynamics in these flows.

A number of studies have used high-resolution numerical models to better understand the dynamics of wave-generated high-concentration mud layers and to address the measurement limitations in the field [*Hsu et al*., 2009; *Ozdemir et al*., 2010a, 2011]. In agreement with the laboratory results, *Hsu et al*. [2009] found that Ri_b is smaller than 0.25, due to either a limited supply of unconsolidated fine sediment and/or a structural difference between tidal currents and wave-driven mudflows. Later *Ozdemir et al*. [2010b] used a numerical simulation in Eulerian-Eulerian framework for low-concentration settings and concluded that fine sediments are well mixed in all phases of the wave, though turbulence is not modulated for such dilute concentration settings. *Ozdemir et al*. [2010a] used the same model for a wide range of suspended sediment concentration (SSC) profiles with fixed wave orbital velocity. They observed a number of different regimes, including no turbulence for very dilute conditions, formation of lutocline, and finally complete laminarization due to strong particle-induced stable density stratification for high sediment concentrations. *Ozdemir et al*. [2011] later investigated the effects of settling velocities, while maintaining constant SSC using the same numerical model. They concluded that larger settling velocity can decrease the thickness of the high-concentration mud layer and eventually cause the flow to laminarize.

In a series of previous laboratory experiments, *Lamb et al*. [2004] investigated the dynamics of high-concentration sediment suspensions with zero slope. Their study [see also *Lamb and Parsons*, 2005; *Liang et al*., 2007; *Yan et al*., 2010] consisted of two series of experiments; one with a rough bed without sediment and one with a sediment bed with mostly silt size particles, representative of a continental shelf seafloor. They found that sediment reduced the thickness of the wave boundary layers substantially but that the flows were still able to support high-density suspensions thicker than the boundary layer due to upward transport of turbulent energy from this thin region. They also suggest that the sediment concentration in the high-concentration layer is sufficient to generate density stratification that may influence the flow dynamics. In their experiments, *Lamb et al*. [2004] and *Lamb and Parsons* [2005] show that waves increase the sand fraction of the near-surface bed layer through winnowing. The coarsened bed surface resulted in significant bed load and the generation of ripples.

Such laboratory investigations of wave-supported gravity currents can bridge between simplified models based on field observations and very detailed numerical models that have not been verified with field measurements. Numerical models still struggle to capture some of the physical processes that are likely to be important in WSGCs [*Hsu et al*., 2009]. In particular, we expect that the range of particle sizes observed in naturally occurring flows contribute to the dynamics of the currents, through the formation of ripples, the generation of density stratification, and the possible interaction of these processes. Numerous studies with sand beds show that turbulence is enhanced due to ripples [*Doering and Baryla*, 2002; *Hare et al*., 2014]. On the other hand, work in exclusively muddy flows shows that suspended sediment can suppress turbulence [*Winterwerp*, 2006]. Continental shelves typically have mostly mud [*Sternberg and Cacchione*, 1996; *Wright et al*., 1997; *Kineke et al*., 2000; *Walsh et al*., 2004] but may include a sand component (0–10%), and both ripples and dense suspensions have been observed [*Ogston and Sternberg*, 1999; *Traykovski et al*., 2007]. The competing effects of ripples and density stratification can enhance or suppress turbulence in the water column. However, it is not known under what conditions bed forms and density stratification will be important in the sediment mixtures typical of WSGCs, whether they will coexist and under which conditions each will dominate. In this work, we will show how ripples and stratification affect the turbulence level in the wave boundary layer and determine the wave conditions in which each of them is dominant.

3. Experiments

The present experiments were carried out in a purpose-built wave-sediment U-tube tank equipped to make high-resolution measurements of velocity, turbulence, and suspended sediment concentration. The experimental facility is the same as the facility used by *Lamb et al*. [2004], with two important modifications. First, it has been modified to extend the upper range of wave periods from 8 to 12 s in order to better simulate waves typically observed on the continental shelf. Second, we use new instrumentation for measuring velocity and sediment concentration that makes high-frequency profile measurements, rather than point measurements, enabling us to better resolve the turbulent wave boundary layer structure.

In order to investigate the relationship between turbulence and suspended sediment in WSGCs we carry out two parallel sets of experiments, one with an active sediment bed and one with a roughened bottom and no sediment. We compare the structure of the turbulence and sediment concentration profiles in the wave boundary layer in both cases.

3.1. Wave Facility

The U-tube wave facility has a sealed 5 m long, 1 m high, and 0.2 m wide test section (Figure 1). Approximately, sinusoidal oscillatory flows in the test section are driven by a moving piston that produces waves with periods of 4–12 s and orbital velocities of 20–70 cm s^{-1}. Rather than wave orbitals, the U-tube facility produces purely horizontal oscillatory mean flows, characteristic of the one-dimensional velocity fields observed near the seabed on the continental shelf due to surface gravity waves. The top and sidewalls of the test section are made of smooth Plexiglas.

3.2. Rough Wall Experiments

For the rough wall (RW) experiments, sand particles ($D_{50}=750\mu$m) were glued to a false floor, which was placed on the bottom of the tank. Clear tap water was used in these experiments, which characterized the turbulent wave boundary layer flow in the absence of sediment. Overall, 20 experiments were performed in

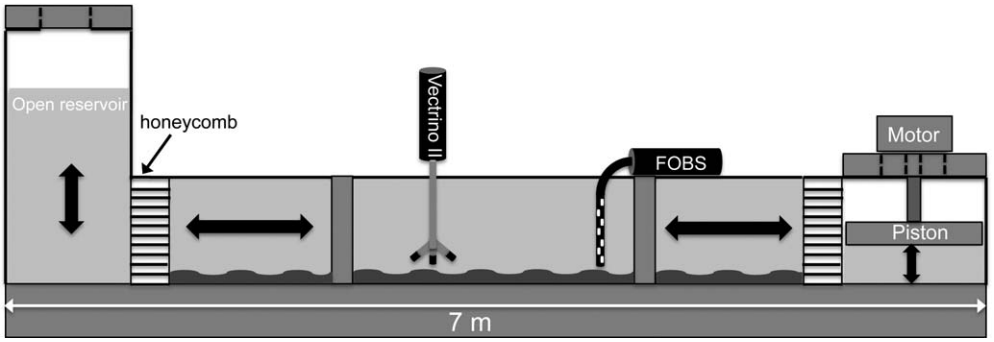

Figure 1. Side-view schematic of wave-sediment U-tube tank. Motion is driven by the piston on the right and return flow from the open reservoir on the left, generating horizontal oscillatory motion in the 0.2 m wide test section.

this mode, which included a range of wave periods ($5 < T < 12$s) and wave orbital velocities ($20 < U_{orb} < 65$ cm s^{-1}). Table 1 shows a summary of the rough wall experiments.

3.3. Sediment Bed Experiments

For the sediment bed (SB) experiments, the false floor was replaced with a 10 cm thick sediment bed. The sediment bed (Sil-co-Sil 106 by U.S. silica) is primarily silt, with clay:silt:sand fractions of 0.10, 0.77, and 0.13, respectively. The sand fraction consists primarily of very fine sand. This distribution is similar to field observations from *Ogston et al.* [2000], who report size fractions of 0.85 clay and silt and 0.15 sand on the northern California continental shelf. A layer of new sediment was added for each run, and the experiment was performed 2 days later to ensure that the degree of consolidation was the same for all experiments. The wave settings covered the same ranges as rough wall experiments. Table 1 shows a summary of the sediment bed experiments.

3.4. Instrumentation

Measurements of the vertical profile of velocity, turbulence, and sediment concentration were made using instrumentation placed in the middle of the test section.

3.4.1. Velocity

Two acoustics Doppler velocimeters (ADV) were used in our experiments. The velocities near the bottom were measured with a profiling ADV (Nortek Vectrino II) which measures three components of velocity (U,

Table 1. Experiments Parameters[a]

Rough Wall Experiments

Run	1	2	3	4	5	6	7	8	9	10	11	12	13	14	15	16	17	18	19	20
U_{orb}(cms^{-1})	35	16	26	30	38	16	19	19	27	35	43	53	19	27	35	44	33	45	57	68
T(s)	4.6	9.4	5.9	5.2	4.3	10	7.8	11.6	7.9	6.3	5.2	4.3	14.6	10	7.7	6.3	10.1	7.4	5.9	5.1
u_*(cms^{-1})	0.6	0.2	0.4	0.9	0.9	0.2	0.3	0.2	0.4	0.7	1	1.3	0.2	0.4	0.8	1.3	0.8	1.1	1.4	1.7
δ(cm)	1.1	0.7	1	0.9	1.1	0.6	0.6	1.3	1.5	1.5	1.5	1.4	1.5	1.5	1.6	1.9	2.4	2.2	2.2	2.2

Sediment Bed Experiments

Run	1	2	3	4	5	6	7	8	9	10	11	12	13	14	15	16	17	18	19	20	21	22	23
U_{orb}(cms^{-1})	37	34	42	57	46	26	30	45	29	42	54	40	15	19	25	32	20	35	23	39	18	26	31
T(s)	8.9	9.6	7.7	5.8	7.1	8.2	7.8	5.2	10.8	7.7	5.9	7.8	10.5	8.6	6.6	5.1	7.9	4.8	7.1	4.4	14.2	9.3	8
u_*(cms^{-1})	1.1	1.1	1.1	0.8	1.4	1	1.1	0.9	1.2	1.2	0.8	1.3	0.6	0.8	1	1.4	0.8	1.2	1.3	1.2	0.9	1.3	1.6
δ(cm)	3.3	3.3	2.9	0.9	3.2	2.5	3	3.4	3.5	3.1	2.7	2.5	1.7	3.6	3.6	1.5	3.6	3.6	3.2	4.6	3	3.4	3.6

Run	24	25	26	27	28	29	30	31	32	33	34	35	36	37	38	39	40	41	42	43	44	45	46
U_{orb}(cms^{-1})	35	39	30	23	34	40	44	50	47	51	26	27	26	25	24	25	24	32	33	32	31	42	42
T(s)	7.3	6.2	10.4	13.7	9.3	7.9	7.1	6.2	6.4	5.6	11.6	11.5	11.6	12.5	12.5	12.4	12.6	9.9	9.8	9.8	9.7	7.7	7.6
u_*(cms^{-1})	1.2	1.3	1.2	0.8	1.3	1.1	1.4	1.2	1.4	1.4	1.1	1.6	0.9	0.8	0.9	0.8	1.1	1.1	1.1	1	1.2	1	1.1
δ(cm)	2.5	3.3	3.2	4.8	3.3	3.1	2.5	2.8	2.8	2.7	3.3	3.9	4.2	3.4	4.2	5.2	4.6	3.4	2.8	3.4	2.5	3.3	2.8

Run	47	48	49	50	51	52	53	54	55	56	57	58	59	60	61	62	63	64	65	66	67	68
U_{orb}(cms^{-1})	40	29	29	29	29	37	37	37	37	37	36	35	36	36	37	36	36	41	44	44	45	44
T(s)	7.8	10.8	10.8	10.9	10.8	8.4	8.4	8.4	8.4	8.4	8.5	8.5	8.4	8.4	8.4	8.5	8.5	7.4	6.6	6.6	6.6	6.7
u_*(cms^{-1})	1.1	1	1.1	1	1.2	1.2	0.9	1.1	1.1	1.5	1.8	1.1	1	1	1.1	1	1.2	1.3	1.1	0.9	1	0.8
δ(cm)	3.7	3.4	3.1	2.8	3.3	2.5	2.5	2.3	2.5	2.1	2.6	3	2.8	2.4	2.3	2.2	2.6	2.9	1.5	1.5	1.9	2.8

[a]Shear velocity (u_*) is derived from the average value of Reynolds stress underneath the wave boundary layer. Wave boundary layer height (δ) is derived from velocity profiles.

V, and W) with a resolution of 1 mm and sampling rate up of 100 Hz. The Vectrino II has a sampling profile of 35 mm (35 bins); however, we use only the middle bins (11–30) due to higher noise near the top and bottom of the ADV profile that affect the turbulence measurements. The other ADV (Nortek Vectrino) was positioned 70 cm from the bottom in the free-stream flow and synced with the Vectrino II in order to detect wave phasing independently of the boundary layer measurements. In each experiment six vertically stacked profiles were acquired with the Vectrino II. These were combined using the wave phase information from the Vectrino in order to generate a 8 cm velocity profile u(z,t).

3.4.2. Sediment Concentration

The concentration measurement was performed with a fiber-optic backscattering sensor (FOBS) and an 11 port vertical sediment siphon rake. The FOBS has 20 bins extending from the bed to 50 cm above the bed, with 1 cm spacing in the lowermost 10 cm and coarser spacing above. The sampling volume is a function of concentration and particle size distribution and varies depending on the SSC in the mud layer. A mixing tank calibration using Sil-co-Sil 106 showed that the FOBS response was linear for concentrations below 80 g L^{-1}, which represents the upper limit of concentrations observed in our experiments based on the sediment siphon data. However, since optical backscatter is very sensitive to the particle size of the suspended sediments [*Downing*, 2006], we also made siphon measurements for many of the experiments. Water and sediment samples were acquired over a 2 min period following the procedure outlined in *Lamb et al*. [2004]. The siphon data provided a redundant measure of the time-averaged concentration profile and were used to calibrate the FOBS output.

4. Turbulence Measurements and Analysis

We used the free-stream ADV as a reference to calculate phase-averaged parameters. These parameters were averaged over 20–50 wave periods giving us phase-averaged data with $\frac{2\pi}{400}$ resolution on the wave period and 1 mm vertical resolution. Phase averaging was done for all parameters, including velocity, production, and Reynolds stress. Wave orbital velocity was calculated according to $U_{orb}=\sqrt{2}U_{rms}$ in which U_{rms} is the root mean square of the velocity +10cm from the bottom. Wave period (T) was calculated using the average value of time differences of occurrence of zero velocities in the velocity time series. Orbital diameter is then defined as the ratio of wave orbital velocity and wave orbital frequency ($\omega=\frac{2\pi}{T}$).

There are two primary independent parameters in our experiments, wave orbital velocity and wave period. Two Reynolds numbers are used to group these two parameters in wave-supported gravity currents, one based on the wave excursion amplitude and the other based on the Stokes boundary layer thickness [*Ozdemir et al*., 2010a]. In this study, we use the latter Reynolds number as our independent parameter since it provides a more convenient length scale for our experiments

$$Re_{\Delta}=\frac{U_{orb}\tilde{\Delta}}{\nu}. \tag{1}$$

Here $\tilde{\Delta}=\sqrt{2\nu/\omega}$ is the Stokes boundary layer thickness and ν is the viscosity.

4.1. ADV Postprocessing

The raw ADV results were quality controlled and the ADV data were despiked using the three-dimensional phase space algorithm developed by *Goring and Nikora* [2002] and *Mori et al*. [2007]. The along-channel, transverse, and vertical velocities were decomposed into wave components $(\bar{u},\bar{v},\bar{w})$ and turbulent fluctuation components (u',v',w'). The vertical and transverse wave components $(\bar{v},\bar{w})$ may be nonzero in the presence of ripples with cross-channel variability. The wave components were separated from the turbulent fluctuation components using a tenth-order Butterworth filter with a cutoff frequency of 1.25 Hz following *Lamb et al*. [2004].

4.2. Turbulent Parameters

The variability and dynamics of the turbulence in the wave boundary layer are quantified in terms of the Turbulent Kinetic Energy per unit mass (TKE)

$$\mathrm{TKE}=\frac{1}{2}(\overline{u'^2}+\overline{v'^2}+\overline{w'^2}) \tag{2}$$

and the TKE evolution equation

$$\mathrm{D(TKE)}/\mathrm{D}t=P+T-B-\epsilon. \tag{3}$$

Equation (3) shows that the rate of change of TKE, $\mathrm{D}(TKE)/\mathrm{D}t$, is determined by the rates of TKE production (P), dissipation (ϵ), transport (T), and the buoyancy flux (B). For uniform steady unstratified currents, $\mathrm{D}(TKE)/\mathrm{D}t$ and B are zero. The integrated TKE transport is often assumed to be negligible, resulting in a balance between P and ϵ. However, there is a phase difference between P and ϵ and these terms do not necessarily balance instantaneously. In fact, the rate of change of TKE can vary by up to 50% of P in low Re_Δ flows due to intermittency in turbulence and transitional flow [*Ozdemir et al.*, 2014]. Furthermore, *Lamb et al.* [2004] suggests that the transport term may be important; it may help to maintain elevated suspended sediment concentration above the defined wave boundary layer. The profiling ADV presents an opportunity to estimate key components of the transport term directly. However, the measurements of the fluctuating velocity gradient were too noisy to reliably resolve this term in our experiments.

We account for noise in the ADV measurements by taking advantage of the redundant vertical velocity measurement on the Vectrino instruments. The noise is much lower in the vertical components compared with the horizontal components due to the geometry of the instrument head. Because of the fourth receiver, the Vectrino II gives us two independent measurements of vertical velocity. We use cospectral analysis of these two measurements to find the variance of the noise in the vertical component and the ADV transformation matrix to determine the noise in the horizontal components. The noise is then subtracted from variance of fluctuation velocity in each component to get the noise free estimates of (u', v', w') and TKE [*Hurther and Lemmin*, 2001].

The Reynolds stress per unit mass $u'w'$ was calculated from the ADV measurements of u' and w', and phased-averaged as described above. The Reynolds stress estimate is inherently noise free, assuming that the noise in the horizontal and vertical velocity components are uncorrelated [*Hurther and Lemmin*, 2001].

The shear velocity $u_*=(\tau_o/\rho)^{1/2}$ (τ_o is the shear stress at the bed) is often estimated based on the law of the wall, $\frac{\partial u}{\partial z}=\frac{u_*}{\kappa z}$. However, applicability of the law of the wall is limited to flows in which the roughness length scale (z_0) is small relative to the wave boundary layer thickness (δ), i.e., $z_0 \ll z \ll \delta$ [*Grant and Madsen*, 1986] and in which density stratification is minimal. Neither of these criteria are satisfied in the present experiments since the flow was not fully turbulent [*Ozdemir et al.*, 2014]. For this reason, we estimate shear velocity based on the Reynolds stress averaged over the wave boundary layer and wave period.

TKE production is calculated using the measured Reynolds stress and vertical velocity gradient according to

$$P \simeq -\overline{u'w'}\frac{\partial U}{\partial z}, \tag{4}$$

where U is the phase-averaged horizontal velocity.

5. The Structure of the Wave Boundary Layer

In this section we investigate the overall structure of the wave boundary layer and the impact of suspended sediment on its structure.

5.1. Velocity Profiles and Wave Boundary Layers

The vertical structure of the velocity profiles in oscillatory flows consists of three distinctive zones: the wave boundary layer zone ($\partial u/\partial z > 0$), the overshoot zone ($\partial u/\partial z < 0$), and the free-stream zone ($\partial u/\partial z \approx 0$) [*Nielsen*, 1992; *Lamb et al.*, 2004]. These three zones are shown for the velocity profile during the maximum velocity phase in Figure 2a. The wave boundary layer (δ) is the point on the border of the wave boundary layer and overshoot zones where the maximum velocity occurs.

The three zones are maintained through each wave phase, but the structure and shear within the boundary layer and overshoot zones are strongly modified. The modification of the wave boundary layer structure within the first half wave period is shown in Figure 2b. The thickness of the wave boundary layer changes

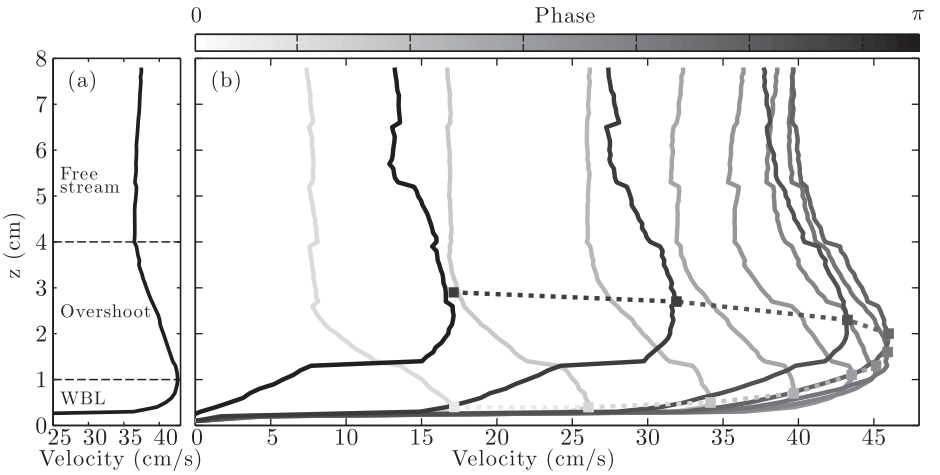

Figure 2. Velocity profiles (a) at maximum velocity phase for a rough wall experiment with U_{orb}=45 cm s^{-1} and T=7.4 s. The velocity profile contains three regions: wave boundary layer, overshoot, and free stream. (b) Wave boundary layer (WBL) growth over a half phase for the same rough wall experiment. The dashed line marks the wave boundary layer height progression and the colors represent the phasing (white corresponds to $t=0$, when the velocity is zero, and black corresponds to $t=T/2$, when flow reversal occurs).

dramatically from 0.3 to 3 cm from the beginning of the wave period until it maximum thickness at flow reversal when a new boundary layer develops. Variations in the maximum velocity and boundary layer thickness result in a peak boundary layer shear that occurs at $t=\frac{T}{8}$.

The wave boundary layer thickness δ is strongly influenced by bed forms and the turbulence level. In Figure 3, δ, estimated based on the velocity and Reynolds stress profiles, is shown for the rough wall and sediment bed runs. The Reynolds stress generally switches sign at the top of the boundary layer because the sign of the shear also changes; thus, δ can also be estimated based on the zero crossing in the Reynolds stress profile. Wave boundary layer height scales with the ratio of shear velocity and wave frequency $(\delta \propto \frac{u_*}{\omega})$ [*Hsu and Jan*, 1998]. In the rough wall experiments, δ increases as U_{orb} increases since u_* increases monotonically as U_{orb} increases. This is consistent with theoretical predictions for wave boundary layer thickness [*Wiberg and Smith*, 1983]. In Figure 3 and subsequent figures, we use Re_Δ, defined in equation (1), as the independent variable because it captures variations in U_{orb} and T; however, variation in Re_Δ primarily reflect variations in U_{orb} because of the stronger functional dependence on velocity and because U_{orb} was varied over a larger range than T. For all but the lowest Re_Δ, the observed boundary layer thicknesses are significantly greater than the analytical solution of the laminar boundary layer thickness $(\delta_{lam} \approx 3.75\sqrt{\frac{2\nu}{\omega}})$.

The boundary layer behaves very differently in the sediment bed experiments compared with the rough wall runs (Figure 3), in part because shear velocity does not increase as U_{orb} increases. For low Re_Δ, δ is 2–4 times greater than in the rough wall runs. As Re_Δ increases above 400–500, however, δ decreases significantly. As will be discussed later, the elevated values of δ for low Re_Δ are attributed to the presence of ripples in this regime and the reduction of δ is attributed to increased density stratification at high Re_Δ, in addition to a decrease in ripple steepness. *Lamb et al*. [2004] and *Ozdemir et al*. [2010a] both observed similar reductions in wave boundary layer thickness and concluded that it was due to stratification. In their DNS runs, *Ozdemir et al*. [2010a] further show that the boundary layer can be laminarized; however, this is not observed in our experiments.

6. Bed Response and Sediment Profile

The addition of an active sediment bed adds two primary components to the wave boundary layer. First, the mobile bed can form ripples and bed forms that increase the roughness of the bed and modify the turbulence in the wave boundary layer. Second, sediment is suspended in and above the wave boundary layer, where it can modify the effective density of the fluid and exert an influence on the turbulence via density stratification. In addition, the high-concentration suspended sediment layer that is generated by the turbulent flow is available to be transported due to its negative buoyancy when the bed is sloped. Here we report the variations in bed forms and the suspended sediment concentration profiles.

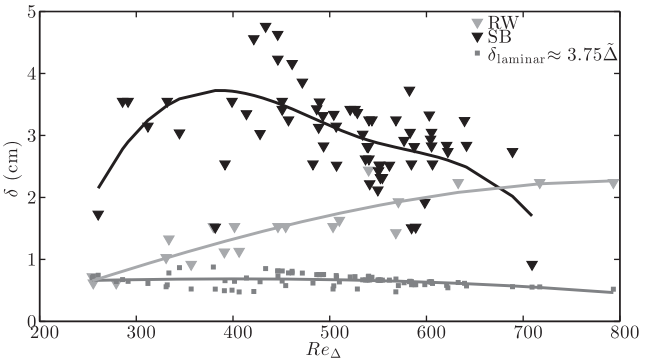

Figure 3. Wave boundary layer height (δ) for rough wall (gray) and sediment bed (black) experiments. Squares and triangles indicate measurements of δ based on the velocity and Reynolds stress profiles, respectively, as described in the text. The thick line is the mean value. The dark gray squares and fit to those data are an estimate of the laminar boundary layer thickness for each experiment ($\delta_{\text{laminar}} \approx 3.75\tilde{\Delta}$), where $\tilde{\Delta} = \sqrt{\frac{2\nu}{\omega}}$ is the Stokes boundary layer thickness.

6.1. Bed Forms

Bed forms play an important role in initiation of sediment suspension, governing the bed shear stress and intensifying near-bed turbulence. They appear in many natural environments and have different shapes and patterns depending on the flow structure and the particle size distribution of the bed. In shallow regions of the inner continental shelf, the dominant bed forms are ripples [*Hanes et al*., 2001]. These ripples typically have irregular two-dimensional forms, similar to those observed in the present laboratory experiments. A few nondimensional numbers have been proposed to determine the criteria for existence of ripples and their steepness, wavelength, and height.

Grant and Madsen [1982] determined ripple type based on the bed shear stress nondimensionalized by the critical shear stress. *Nielsen* [1981] and *Van Rijn* [1993] used the mobility number defined as $\psi = \frac{U_{orb}^2}{sgD_{50}}$ where $s = 1.65$ is the submerged weight of sediment relative to water and D_{50} is the median size for sediment particles. *Wiberg and Harris* [1994] used near-bed orbital diameter $(d_0 = \frac{2U_{orb}}{\omega})$ nondimensionalized by the ripple height $(\frac{d_0}{\eta})$ where η is ripple height.

Ripples are observed in almost all of our sediment bed experiments, and their morphology changes as the flow forcing is varied. We interpret these changes following *Wiberg and Harris* [1994], who suggested that ripples be classified into three types based on the dimensionless orbital diameter d_0/η. Here $d_0 = \frac{2U_{orb}}{\omega}$ is the orbital diameter and η is the ripple height. According to the *Wiberg and Harris*'s [1994] classification scheme, orbital ripples are observed when $d_0/\eta < 20$ and have wavelengths proportional to the wave orbital diameter. Anorbital ripples are observed when $d_0/\eta > 100$ and have wavelengths proportional to the grain size and independent of orbital diameter. Finally, suborbital ripples are observed when $20 < d_0/\eta < 100$ and have wavelengths that are not proportional to the orbital diameter or grain size.

The ripple height and wavelength λ in our experiments were estimated from multiple photographs taken through the tank wall during each experiment. The ripple steepness η/λ was then calculated and averaged over the experiment period. Almost all of the ripples observed in our experiments were in the anorbital range (Figure 4a). The curve suggested by *Wiberg and Harris* [1994] captures our data relatively well; however, it overestimates the ripples steepness for high d_0/η. Note that while the sediment that was used in the sediment bed runs was mostly fine silt ($D_{50} = 23\mu$m), *Lamb and Parsons* [2005] showed that the sediment in the ripples consist primarily of sands ($D = 70\mu$m) as a result of sediment bed coarsening. *Lamb and Parsons* [2005] used similar sediment and the same flow facility for their experiments.

We observe that ripple steepness decreases with increasing wave forcing (Re_Δ), consistent with the findings of *Wiberg and Harris* [1994] (Figure 4b). Higher wave orbital velocities suspend more sediment and this higher proportion of sediments in suspension is associated with a decrease in ripple steepness [*Wiberg and Harris*, 1994]. The range of ripple heights, from 1 to 10 mm, is well below the wave boundary layer height $(\eta/\delta_w < 0.25)$, consistent with the characterization of the bed forms as anorbital ripples; orbital ripple heights are larger than the wave boundary layer $(\eta/\delta_w > 2)$ [*Wiberg and Harris*, 1994]. The ripple height, wavelength, and steepness observed in our experiments are in the same range as those reported in previous experiments [*Lamb and Parsons*, 2005; *Van Rijn*, 2007; *O'Donoghue et al*., 2006; *Vongvisessomjai*, 1984].

6.2. Suspended Sediment Concentration

The observed suspended sediment concentration (SSC) profiles for the sediment bed experiments decrease approximately exponentially from their peak value at the bed to a constant background value far from the bed, which is due to mixing in the end tanks (Figure 5). We designate C_a as the near-bed concentration and C_b

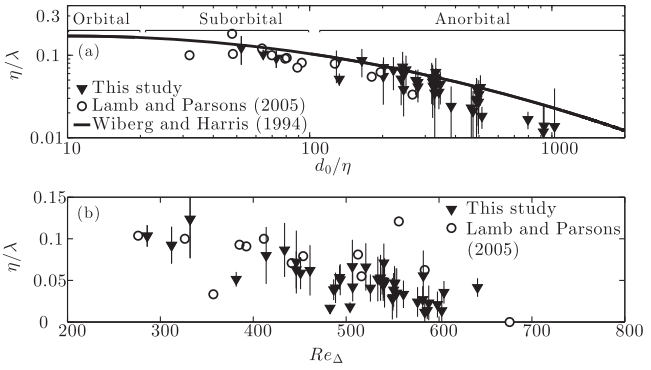

Figure 4. (a) Ripple steepness versus nondimensional orbital diameter for sediment bed experiments. The vertical lines are the standard deviations based on the variability within each experiment. The three ripple classifications and the predictive model developed by *Wiberg and Harris* [1994] are shown with over brackets and the black line, respectively. (b) Variation of ripple steepness with Reynolds number. Error bars are based on the range of ripple steepness observed within each run.

as the background concentration. For each experiment, a SSC profile in the form of $c(z)=C_b+C_a e^{-\alpha z/h}$ was fit to the data. In this study, although we see high sediment concentrations similar to those observed in the field, the structure of the near-bed sediment profile does not display the uniform SSC layer below the lutocline observed in some field studies [e.g., *Cacchione et al*., 1995; *Ogston et al*., 2000]. Instead, the concentration always increases exponentially toward the bed similar to experimental and field observations of *Lamb et al*. [2004] and *Traykovski et al*. [2007]. Here we define the lutocline (h) as the point where the SSC is $0.05C_a$. Therefore, α is chosen to be 3 to satisfy this condition. The background concentrations (C_b) in all experiments are subtracted from SSC profiles for further analysis since it is the vertical density gradient, rather than the absolute value, that influences density stratification. Elevated sediment concentrations may influence the effective viscosity of the fluid [*Traykovski et al.*, 2015]; however, this effect is only significant in the two highest experiments and will be discussed in a future paper. For the low-velocity experiments, relatively less sediment is in suspension and the near-bed layer is relatively dilute. As the wave orbital velocity increases, SSC increases and a clear high-concentration layer is observed. The dilute and high-concentration sediment suspension regimes in wave-supported flows were also observed experimentally by *Lamb et al*. [2004] and in the field by *Traykovski et al*. [2007].

In Figure 6, the height of the lutocline, near-bed SSC, and average SSC gradient inside the high-concentration layer are shown. The height of the lutocline decreases as the wave orbital velocity increases (Figure 6a). Note that there is quite a bit of scatter in the lutocline heights at low Re_Δ because the concentration gradient at the top of the layer is much smaller. In all of our experiments, the lutocline height was greater than the wave boundary layer, which suggests that turbulence may be transported vertically to regions above the wave boundary layer [*Lamb et al*., 2004]. The lutocline heights in our experiments are similar to those observed in the field by *Traykovski et al*. [2007]. For our experiments h/δ was approximately 3.2 ± 1.8. The lutocline height decreases with increasing Re_Δ, consistent with the observed decrease in δ (Figure 3). The generation of a high-concentration mud layer with increasing wave intensity is clear in Figures 6b and 6c, which show that both near-bed reference SSC (C_a) and sediment concentration gradient increase dramatically when Re_Δ exceeds a critical value of approximately 450. The near-bed SSC and SSC gradient are both constant and small for low Re_Δ and increase when $Re_\Delta > 450$, eventually reaching values 3–4 times greater than those at low Re_Δ. The threshold for the generation of a high-concentration mud layer in our experiments corresponds to a wave orbital velocity of approximately $25-30$ cm s^{-1}. This is consistent with the threshold observed by *Lamb et al*. [2004]; they report that no high-density suspension layer is generated in their experiments when the wave orbital velocities were smaller than 30.3cms^{-1} (run S4 in their paper).

7. Turbulence in the Wave Boundary Layer

7.1. Reynolds Stress

The phase-averaged near-bottom Reynolds stress is shown in Figure 7 for an example rough wall run ($U_{orb}=57$ cm s^{-1} and $T=5.8$ s). At flow reversal (zero phase) the Reynolds stress very near the bottom is close to zero. As the wave velocity increases, the magnitude of the opposing near-bottom stress increases, reaching its maximum value at maximum velocity phase. The thickness of the high-stress layer increases slowly immediately after flow reversal and then increases more rapidly until the subsequent flow reversal. After flow reversal the very near-bottom stress goes to zero as it switches sign, but significant stress from

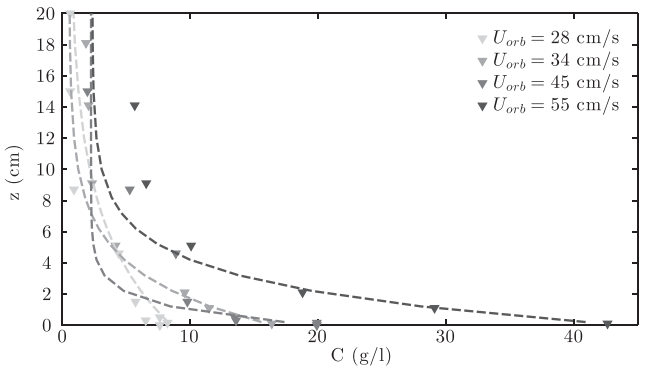

Figure 5. Suspended sediment concentration profiles for experiments with different wave orbital velocities. The points show the data from siphon measurements and the lines are the best fit to the data in the form of $c(z)=C_b+C_a e^{-3z/h}$.

the preceding wave phase persists as a residual stress. This residual stress has the opposite sign of the very near-bottom stress and continues to penetrate upward well above the height of the wave boundary layer. The residual stress generally persists for a half wave period after flow reversal, though low levels of residual stress are sometimes observed after even longer periods (Figure 7).

The height of the wave boundary layer, δ, based on the velocity maximum is shown in Figure 7 (black line). It is clear that there is very good correspondence between the observed Reynolds stress profiles and δ; the top of the boundary layer separates the near-bottom boundary layer stress from the residual stress that persists from the previous wave phase. The upward penetration of turbulence may provide a mechanism for transport of sediment from the wave boundary layer into the overlying fluid. We will see, however, that the residual stress is less intense in the sediment bed runs, especially in runs with a high-concentration mud layer.

In Figure 8 we present the Reynolds stress for five rough wall runs with increasing Re_Δ (increasing U_{orb}) and corresponding sediment bed runs with the same wave settings. For the rough wall runs, the Reynolds stress is very low when Re_Δ is low (Figure 8a) and increases gradually as Re_Δ increases (Figures 8b–8e). The wave boundary layer also gets thicker as Re_Δ increases and we observe that the transition to a thicker boundary layer occurs earlier as Re_Δ increases.

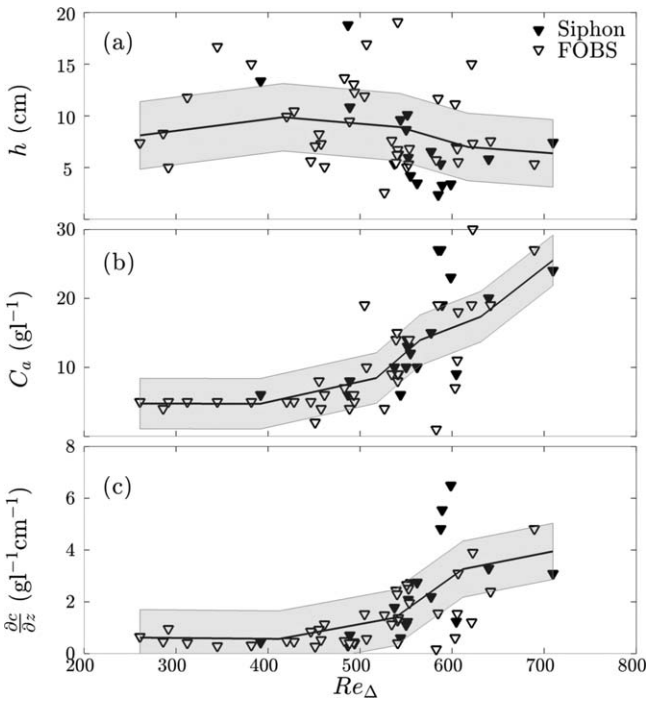

Figure 6. High-concentration mud layer (a) thickness h, (b) near-bed concentration C_a, and (c) concentration gradient. All values are derived from the fit to the concentration profiles using $c(z)=C_b+C_a e^{-3z/h}$. The black and white triangles show measurements using the siphon or FOBS, respectively. The solid lines are the bin-averaged values and the shaded areas show the standard deviation around the averaged values.

We observe a very different evolution in the Reynolds stress in the corresponding sediment bed experiments. First, the Reynolds stress is significantly more intense and the wave boundary layer is thicker in the low Re_Δ sediment bed runs (Figures 8f and 8g) than in the corresponding rough wall runs (Figures 8a and 8b). The elevated stress at low Re_Δ is most likely due to the occurrence of bed forms in this regime, as discussed below. Second, while Reynolds stress and δ increase uniformly with Re_Δ in the rough wall runs, they appear to decrease slightly in the high Re_Δ sediment bed runs (Figures 8h–8j). This decrease is observed for runs with $Re_\Delta > 450$ ($U_{orb} > 30$ cm s^{-1}) when we observe that the high-concentration mud layer forms, suggesting that it is associated with turbulence suppression

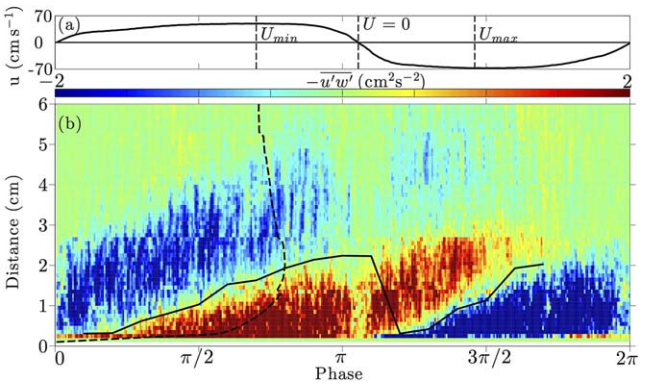

Figure 7. (a) Free-stream velocity and (b) Reynolds stress (cm^{2}s^{-2}) for a rough wall with U_{orb} = 57 cm s^{-1} and T = 5.8 s. The vertical dashed lines indicate the minimum, zero, and maximum-velocity phases. The solid lines indicate the boundary layer height derived from the height of the maximum velocity. The curved dashed line shows a sample velocity profile at $t = \frac{3T}{8}$.

due to stratification. Finally, we observe that the residual Reynolds stress has lost its intensity due to dissipation and/or diffusion earlier in the high Re_Δ sediment bed runs, relative to the rough wall runs. As discussed in section 6.2, the height of the lutocline is typically 3–4 times greater than δ; thus, it is likely that the reduction in residual stress in the sediment bed runs is due to the persistence of sediment stratification above the wave boundary layer.

We define the shear velocity $u_* = (\overline{-u'w'})^{1/2}$ as the maximum Reynolds stress in the boundary layer (Figure 9), which enables us to more easily

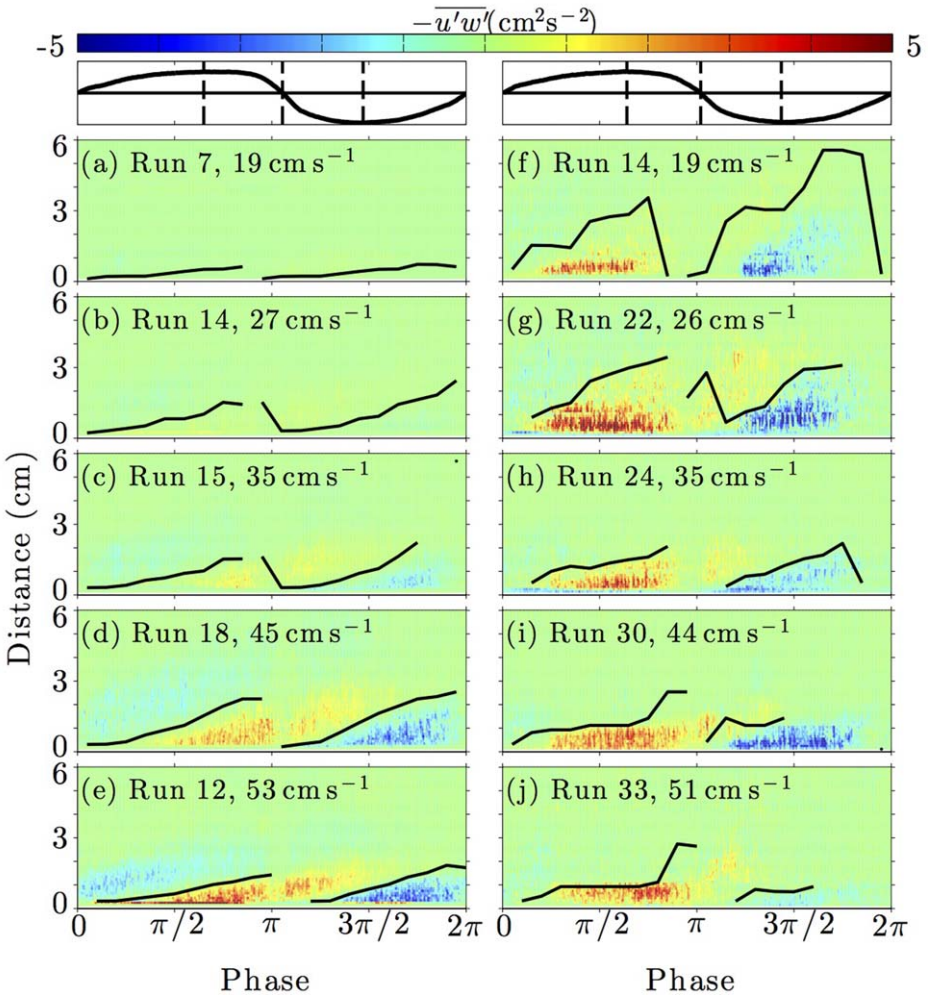

Figure 8. (a–e) Reynolds stress for the rough wall and (f–j) the sediment bed runs. The top two figures show the free-stream velocity with the minimum and maximum velocity and flow reversal times indicated by vertical-dashed lines. The rough wall and sediment bed experiments in each row have similar wave orbital velocities (U_{orb}), which is indicated in the caption for each figure. Solid black lines in each figure show boundary layer heights derived from the maximum velocity.

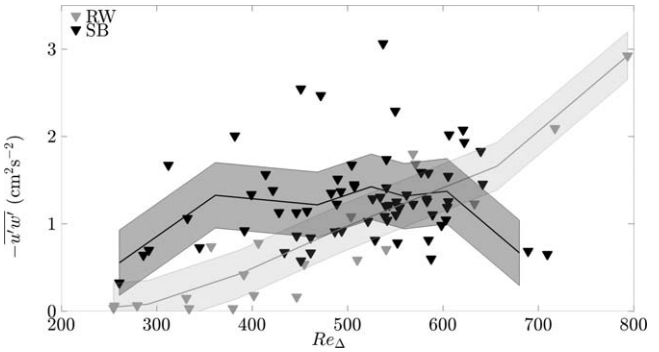

Figure 9. Comparison of average Reynolds stress for rough wall (gray) and sediment bed (black) runs. Average Reynolds stress is defined as the maximum of vertically averaged Reynolds stress in the wave boundary layer over the wave period, as described in the text.

compare and quantify the differences in behavior between the rough wall and sediment bed runs observed in Figure 8. We calculate u_* based on the vertical mean between the bed and the top of the wave boundary layer and the temporal maximum over a wave period. In the rough wall runs, u_* increases monotonically with Re_Δ, as expected [e.g., *Nielsen*, 1992]. For the sediment bed runs, u_* is initially elevated and then appears to stay constant or decrease as Re_Δ increases. When $Re_\Delta < 450$ ($U_{orb} < 30$ cm s^{-1} for a 8 s wave), the shear velocity is approximately 3–4 times larger in the sediment bed runs than in the rough wall runs. This elevated stress is associated with the presence of larger, steeper ripples in this regime (Figure 4b). In this regime we also observe an increase in u_* with increasing the wave orbital velocity, which is approximately similar to the rate observed in the corresponding rough wall experiments. When $Re_\Delta > 450$ ($U_{orb} > 30$ cm s^{-1} for a 8 s wave), u_* remains constant or decreases as Re_Δ increases, eventually resulting in lower values of u_* in the sediment bed runs relative to the rough wall runs at the highest Re_Δ values. In this range, although small, long-wavelength ripples still exist, turbulence suppression due to vertical density stratification in the sediment bed experiments appears to be sufficient to reduce the shear velocity below that observed in the rough wall experiments.

The temporal variability and magnitude of the shear velocity that we observe in our rough wall runs is consistent with experiments by *Hay et al*. [2012a]. However, the observed magnitudes are smaller than those observed in the field [*Traykovski et al*., 2007], possibly because we use the maximum depth averaged Reynolds stress in the boundary layer to determine shear velocity instead of law of wall or wave friction coefficient.

7.2. Turbulent Kinetic Energy

The results in section 7.1 describe how the presence of sediment can increase or decrease the turbulent stress and motivate the need for a clear understanding of the turbulent dynamics in high sediment concentration wave boundary layers. The turbulent kinetic energy (TKE) and TKE production rate (P) for the rough wall and sediment bed experiments are shown in Figure 10. As with the Reynolds stress, TKE and P are averaged spatially over the height of the boundary layer and temporally over one wave period. The comparison between the rough wall and sediment bed values for both of these parameters is generally similar to the results obtained with Reynolds stress; TKE and P both increase monotonically in the rough wall experiments, whereas they are both elevated in the sediment bed experiments for low Re_Δ and reduced for high Re_Δ, relative to the corresponding rough wall values. Both TKE and P are relatively constant across a wide range in Re_Δ, although P appears to decrease slightly in magnitude. At low Re_Δ, P is approximately 1 order of magnitude greater in the sediment bed runs than in the corresponding rough wall runs.

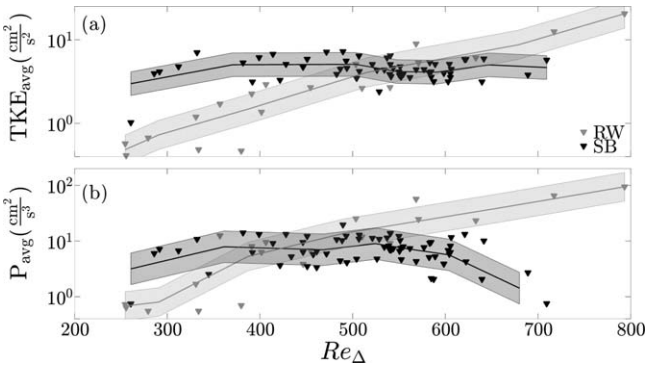

Figure 10. Average (a) turbulent kinetic energy and (b) turbulent kinetic energy production within the wave boundary layer for rough wall (gray) and sediment bed (black) runs. The solid lines are the bin-averaged values and the shaded areas show the standard deviation around the averaged values.

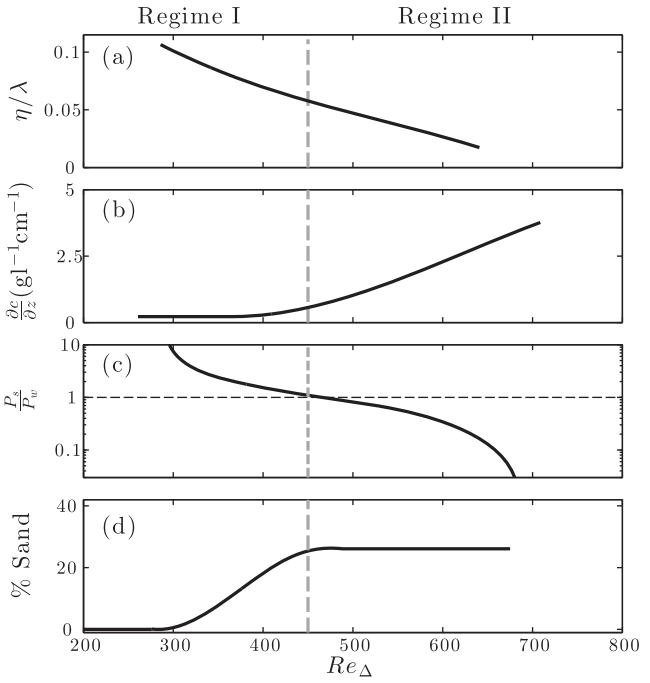

Figure 11. Summary schematic comparing the trends in key parameters observed to be important in the dynamics of wave-supported mud layers. Each figure presents the fit to the data shown elsewhere in the paper. (a) Ripple steepness, (b) near-bed vertical sediment concentration gradient, (c) ratio of TKE production in the sediment experiments (P_s) to the rough wall experiments (P_w) from equation (5), and (d) average-suspended sand fraction below 10 cm based on data from *Lamb and Parsons* [2005]. The vertical line at $Re_\Delta = 450$ indicates the approximate transition between Regime I and Regime II.

8. Discussion

Understanding the physical details of wave-supported mudflows is a key step in improving our prediction of sediment transport across the continental shelf. High-resolution measurements of the dynamics of these flows are challenging in the field because they have relatively small vertical scales and are very episodic in nature. The present laboratory experiments simulate the conditions under which wave-supported mudflows occur on the continental shelf and use detailed measurements of velocity and turbulence with and without sediment to understand the relationship between bed dynamics, suspended sediment, and turbulence in the wave boundary layer. Our overall goal is to clarify the processes that determine the vertical profiles of suspended sediment and velocity in wave-supported mud layers in order to improve models of cross-shelf sediment transport.

The qualitative character and the dominant dynamics of the observed flow vary significantly across the parameter space of our experiments and suggest that the flow should be described in two distinct regimes. The regimes are differentiated in terms of the Stokes Reynolds number (Re_Δ) and the primary attributes are summarized schematically in Figure 11, which summarizes the key measurements from the present experiments. Regime I occurs when $Re_\Delta < 450$, which corresponds approximately to $U_{orb} < 30$ cm s^{-1}. The flow in this regime is dominated by the presence of ripples and characterized by a dilute sediment suspension; no high-concentration mud layer or distinct lutocline forms (Figures 11a and 11b). The turbulent kinetic energy production is significantly higher in the sediment bed experiments compared with corresponding rough wall experiments as a result of the increased bed roughness associated with ripple formation (Figure 11c). For all experiments in this regime, the near-bed sediment concentration and vertical concentration gradient were low and approximately constant with respect to Re_Δ, suggesting that density stratification effects were minimal (Figure 11b). Regime II occurs when $Re_\Delta > 450$. Flow in this regime is dominated by the formation of a high-concentration mud layer and the associated vertical density stratification dominates the dynamics. The ripples are approximately half as steep as they are in Regime I, and their importance to the overall dynamics appears to be small (Figure 11a). The magnitude of TKE and P are smaller in the sediment bed experiments than in the corresponding rough wall experiments (Figure 11c). It is important to note that the ripples do not disappear completely in the high Re_Δ runs and so the bed remains rougher than in the rough wall runs. Thus, the facts that the turbulence levels in the sediment bed experiments do not increase with Re_Δ and remain below the levels of the rough wall experiments cannot be explained by the change in bed roughness alone. Strong density stratification (Figure 11b) appears to be effective at suppressing turbulence in the wave boundary layer and reducing the wave boundary layer thickness. Turbulence near the upper boundary and above the wave boundary layer can be completely suppressed due to this high-density stratification.

The present experiments confirm and extend some of the conclusions in *Lamb et al.* [2004] and *Lamb and Parsons* [2005] and also provide some notable differences. Their results support the definition of the two

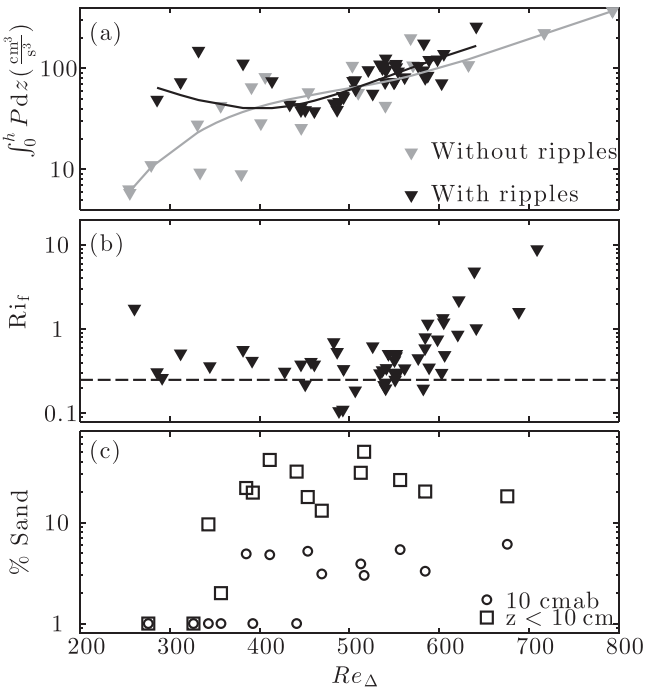

Figure 12. (a) Depth-integrated production based on roughness scales observed in the rough wall (gray) and sediment bed (black) experiments. The values represent predictions of the production based on the observed U_{orb} and ripple steepness. The lines are spline fits intended to illustrate the overall trend. (b) Flux Richardson number defined as the ratio of buoyancy flux to TKE production rate where buoyancy was estimated using eddy diffusivity from *Thorne et al*. [2009]. (c) Sand fraction at 10 cmab and the average sand fraction below 10 cmab from the experiments of *Lamb and Parsons* [2005].

regimes described above; they also observe that no high-concentration layer forms for low U_{orb} (corresponding to low Re_Δ) and suggest that density stratification is important for reducing the boundary layer thickness in sediment bed runs with higher U_{orb}. *Lamb and Parsons* [2005] describe ripple formation and their results, which are replotted in Figure 4b, are consistent with the present results, also showing that ripple steepness decreases for high Re_Δ (Regime II). *Lamb et al*. [2004] report that turbulence suppression associated with density stratification resulted in wave boundary layers smaller than 3 mm, which approaches the thickness expected for laminarization of the boundary layer. This magnitude of boundary layer reduction was not observed in our experiments. In fact, while we do observe a decrease in δ as stratification increases, δ is higher in almost all of the sediment bed runs than it is in the corresponding rough wall runs. We expect that this difference in δ between our results and *Lamb et al*. [2004] is probably due to the increased resolution provided by the profiling ADV used in the present study compared with *Lamb et al*.'s [2004] point-wise velocity measurements. A central conclusion in *Lamb et al*. [2004] is that there is a large mismatch between the thickness of the mud layer and boundary layer, which requires that there is significant upward transport of turbulence from the thin energetic boundary layer region to maintain suspension of sediment in the region above the boundary layer. We also observe that $h > \delta$, though the mismatch is only a factor of 3–4 in our observations. However, we were not able to confirm the importance of the turbulent transport term with our measurements. Finally, *Lamb and Parsons* [2005] point to the important role that sorting of grains of different size may play in the dynamics of the mud layer as U_{orb} increases. In section 8.3 we discuss the importance of the suspended sand fraction in our observations.

8.1. Ripples

Ripples were observed in most of the sediment bed experiments and appear to play an important role in generating turbulence, especially at low Re_Δ. Ripples emerge in systems with an active bed load layer and thus require a minimum amount of sand on the bed [*Wiberg and Harris*, 1994]. Although our initial sediment bed contained primarily silt-size particles, segregation of sand as a result of the suspension of clays and fine silts coarsened the sediment bed, resulting in a significant active bed load layer and supporting the formation of ripples. This process is described in more detail in *Lamb and Parsons* [2005]. Ripples change the bottom roughness significantly, which can increase the turbulence in the wave boundary layer and the boundary layer thickness. In the present experiments steep ripples were observed in low Re_Δ conditions. As Re_Δ increases the ripples steepness decreases by an order of magnitude from 0.1 to 0.01. The existence of ripples can significantly change the vertical structure of the velocity field and turbulence in and outside of the wave boundary layer. *Doering and Baryla* [2002] showed that the velocity field is strongly influenced by the presence of ripples in their experimental wave flume. They concluded that ripples can strongly

influence the velocity structure in a region above the ripples that is 2–4 times the ripple height. In our low Re_Δ experiments, the observed boundary layer heights are 3−4cm compared with ripple heights of 0.1−1cm. This is consistent with the upward penetration of ripple-generated turbulence observed by *Doering and Baryla* [2002] and suggests that the enhanced thickness of the wave boundary layer in our low Re_Δ sediment bed experiments is a result of ripples.

We test this further by computing the predicted TKE production with and without ripples (Figure 12a) and comparing this with our observations. The prediction uses only the observed wave orbital velocity and period and varies the bed roughness based on the observed ripple heights. It isolates the effect of the ripples on boundary layer turbulence and does not account for density stratification. The depth integrated production is estimated according to

$$P_k = \beta u_*^2 U_{orb}, \tag{5}$$

in which β is chosen to be 0.3 based on our experimental results. The shear velocity is $u_* = \sqrt{f_w/2}U_{orb}$, in which the wave friction coefficient is estimated following *Nielsen* [1992] from

$$f_w = \exp\left(5.5(r_h/A)^{0.2} - 6.3\right), \tag{6}$$

where $A = U_{orb}/\omega$ is the wave excursion amplitude of the interior flow immediately outside the boundary layer and r_h is the hydraulics roughness of the bed. For the rough wall experiments, r_h is chosen to be the size of the sand grains on the rough bottom, D_{50}=0.75mm. These results agree qualitatively with the average TKE and production measured in our experiment for $Re_\Delta < 450$ (Figure 10b). For the sediment bed experiments, the observed ripple amplitudes and wavelengths were used to compute the roughness based on $r_h = 24\eta^2/\lambda$ [*Thorne et al.*, 2002; *Hay et al.*, 2012b]. The predicted TKE production increases monotonically in rough wall experiments as expected (Figure 12a). When ripples are present, the production is significantly higher than in the corresponding rough wall runs, as observed in our measurements (Figure 10). This comparison further confirms that the observed enhancement of turbulence for low Re_Δ is due to ripples. However, when $Re_\Delta > 450$ and the ripple steepness decreases, the predicted TKE production continues to increase in the ripple runs and is comparable to the production in the rough wall runs (Figure 12a). This prediction is in contrast to the high Re_Δ measurements, in which the production is significantly lower in the sediment bed runs than in the rough wall runs (Figure 10b). Thus, the prediction shows that production should increase for high Re_Δ even though most of the ripples are washed out and another process is required to explain the observed suppression of turbulence. In the following section we discuss the role of density stratification in suppressing turbulence in the wave boundary layer.

8.2. Stratification

Density stratification associated with high near-bed sediment concentrations can suppress turbulence in highly stratified flows [*Winterwerp*, 2006]. In oscillatory boundary layers, high-density stratification may decrease the wave boundary layer thickness and turbulence intensity. Although the turbulence level is dramatically reduced, the turbulent energy is sufficient to maintain particle suspension in such highly stratified layers primarily due to hindered settling [*Winterwerp*, 2006].

The numerical model results of *Ozdemir et al.* [2010a] suggests that turbulence suppression associated with high-concentration fluid muds may be sufficient to laminarize the wave boundary layer. They investigate the effects of fine sediment on turbulence in the vicinity of the river mouths where the amount of river-borne sediment varies significantly. The wave conditions were the same for all their runs and similar to typical coastal settings; the wave orbital velocity and period were 56 $cm\,s^{-1}$ and 8.6 s, respectively, resulting in $Re_\Delta \approx 1000$. They performed four runs with zero, low, medium, and high sediment concentrations. In the low-concentration runs, the near-bed sediment concentration was 10 $g\,L^{-1}$, turbulence was attenuated near the top of the wave boundary layer due to density stratification but turbulence near the bed was unaffected. The maximum wave boundary layer was similar to the zero-concentration run (δ=2.8 cm). For the medium-concentration run, the near-bed sediment concentration was 50 $g\,L^{-1}$, turbulence was attenuated in the entire wave boundary layer, wave boundary layer thickness was significantly reduced (δ=0.7cm), and the velocity profile was very similar to that observed in a laminar flow. However, instabilities were observed near the lutocline and the flow was not completely laminarized. For the high-concentration run, the near-bed sediment concentration was 100 $g\,L^{-1}$ and the velocity structure and wave boundary layer thickness

were similar to the medium-concentration run. However, there were no instabilities and the flow was completely laminarized.

The present experiments span a similar parameter range to the simulations in *Ozdemir et al*. [2010a] and so they provide a good test of the model predictions. There are two important differences in the experimental setup; the background sediment concentration in the numerical model experiments is initially prescribed and independent of the wave settings since the model is designed to simulate direct input from rivers. However, the initial sediment conditions are identical in each of our laboratory experiments since the only source of suspended sediment is erosion from the bed and only the wave settings are varied. As a result, the near-bed sediment concentrations are determined entirely by the wave forcing. Also, the model runs consist of a single grain size equivalent to a silt-sized particle. This is expected to lead to a few possible differences in the behavior of the model and experiments, most notably that no bed roughness forms in the model.

There are a number of indications that density stratification is important in suppressing turbulence in our experiments. The wave boundary layer thickness decreases significantly when the flow becomes highly stratified at high Re_Δ (Figure 3). We also observe that turbulence in upper regions of the wave boundary layer is increasingly attenuated as stratification increases, as observed by *Ozdemir et al*. [2010a]. TKE and its production rate in the wave boundary layer remain relatively constant and significantly lower than the corresponding rough wall values at high Re_Δ (Figure 10). Although the ripple steepness is significantly reduced in this regime, the bed roughness remains much higher than that in the rough wall experiments and so the turbulence intensity is expected to be as high or higher in the absence of stratification. Thus, these results also suggest that density stratification is effective at suppressing turbulence, by approximately an order of magnitude relative to the rough wall experiments, at high Re_Δ.

In Figure 12b, we show the flux Richardson number (Ri_f) results for the experiments where Ri_f is the ratio of buoyancy flux to TKE production. The buoyancy flux was estimated using a linear eddy diffusivity with the form of $\epsilon_s = \frac{3\sqrt{2}}{10}\kappa u_* z$ [*Thorne et al*., 2009] and SSC gradients. The coefficient was chosen to take into account the different approaches that this study and *Thorne et al*. [2009] use in shear velocity estimation. Turbulent shear flows collapse when Ri_f exceeds a critical value Ri_c, where the energy required to mix sediment over the water column is more than the available kinetic energy provided by the flow [*Turner*, 1973; *Winterwerp*, 2006]. As a result, the flow becomes more stratified and cannot mix. We observe that Richardson numbers maintain a critical value close to $\frac{1}{4}$ for $Re_\Delta < 550$. This critical value is consistent with the observations of *Trowbridge and Kineke* [1994] and close to 0.15, the prediction of *Turner* [1973] for critical flux Richardson number. When $Re_\Delta > 550$, the flux Richardson number exceed the critical value and the flow becomes more stratified. This region likely corresponds to the supersaturated conditions described by *Winterwerp* [2006] where we anticipate a collapse of the concentration profile and of the turbulent flow field.

Despite the strong turbulence suppression, we do not observe any evidence of laminarization of the flow in our data, however. TKE was always significant in the wave boundary layer, even in highly stratified conditions and the wave boundary layer was always much thicker than what would be expected for laminar flow. One likely explanation for this is that there is always some roughness on the sediment bed in the experiments, whereas there is no perturbation except the initial condition in the *Ozdemir et al*. [2010a] simulations. Perhaps more importantly, the sediment concentration is a result of the wave forcing in the experiments, instead of an independent prescribed parameter. Altering wave conditions can change the concentration threshold required for complete laminarization dramatically. *Baas et al*. [2009] showed experimentally that doubling the velocity increased the threshold sediment concentration necessary for laminarization eightfold. Although their experiments were not in wavy environments, one can assume that similar trends might be applicable to wave boundary layers. Thus, we expect that the threshold for laminarization will continue to increase as the wave forcing increases, even as the near-bed sediment concentration also increases.

8.3. Transitional Behavior and the Role of Fine Sand

The results summarized in Figure 11 and associated discussion indicate that the flow undergoes a transition when $Re_\Delta \approx 450$; high-concentration layers can only form when Re_Δ exceeds this threshold. It is instructive to investigate the dynamics leading to this threshold behavior. Our results support the hypothesis that the threshold near $Re_\Delta = 450$ is a consequence of increases in the concentration of fine sand in suspension, which generate higher near-bed stratification, and decreases in ripple steepness.

In Figure 12c, the average sand fraction in the water column is shown based on the measurements of *Lamb and Parsons* [2005] who performed very similar experiments in a modified version of the same facility as the present experiments. We show the average sand concentration 10 cmab and the average value below it. The fine sand concentration in the water column is close to zero for low Re_Δ. Above $Re_\Delta = 300$ the amount of sand suspended near the bed increases dramatically until it reaches close to 25% for $Re_\Delta > 450$. This shift results in a higher settling velocity and settling flux in the high-concentration layer, increasing the near-bottom stratification. Also, because turbulence is low above the boundary layer, fine sand particles are primarily limited to the boundary layer, further increasing the stratification, especially at the top of the layer. The intensified stratification likely suppresses turbulence, leading to a feedback that contributes to collapse of the layer thickness.

The sand dynamics may also influence the transition through their impact on ripple formation. Below $Re_\Delta = 450$, the prevalence and influence of ripples indicates that the bed dynamics are dominated by bed load transport. Although the initial sand fraction of the bed was only approximately 10%, *Lamb and Parsons* [2005] show that winnowing results in sand fractions of 30–70% (their Table 1) on the bed for $Re_\Delta < 450$. As Re_Δ increases above 300, more and more sand is entrained into the water column from the bed load layer. This corresponds to a decrease in ripple steepness, which likely contributes to the observed transition.

It is important to note that the dynamics are probably more complicated than the description above due to the complexity of the sediment interactions in clay-silt-sand mixtures. Even when the sediment bed consists primarily of sand the clay fraction can form a cohesive layer around the sand particles, resulting in significant cohesive forces [*Van Rijn*, 2007]. When the sediment bed mixture consists primarily of finer particles, the exact mechanism for sediment suspension is also difficult to characterize since silt particles typically erode as aggregates in the form of chunks rather than individual particles [*Roberts and Jepsen*, 1998]. Visual observations from our experiments are consistent with this description; sediment is initially suspended in chunks, although it is likely that the chunks disaggregate after erosion.

The details of the suspension process cannot be fully resolved in our experiments. However, the observed behavior strongly supports the conclusions that the threshold condition necessary for the generation of high-concentration sediment layers is controlled largely by the character of the bed, and especially the fine sand content. It follows that the threshold value of Re_Δ, observed here to be 450, is probably a function of suspended sand concentration. As a result, the threshold conditions necessary for transport of sediment in wave-supported gravity currents will likely vary based on the grain size distribution in the bed deposit.

9. Summary and Conclusions

We carried out comprehensive, high-resolution measurements of velocity, turbulence, and suspended sediment concentration in a wave flume in order to describe the physical processes that control the formation of wave-supported high-concentration mud layers and associated gravitational transport on the continental shelf. Our results support the following conclusions:

1. No high-concentration sediment layer forms in Regime I, which corresponds to $Re_\Delta < 450$. In this regime, ripples dominate the bed dynamics, enhancing near-bed turbulence and increasing the wave boundary layer thickness. Turbulent kinetic energy is 2–3 times higher than corresponding rough wall experiments with similar wave conditions.
2. A high-concentration sediment layer forms in Regime II, corresponding to $Re_\Delta > 450$. In this regime, the ripple steepness is small and the stratification due to increased fine sand content in suspension suppresses the turbulence. Turbulent kinetic energy is lower than it is in corresponding rough wall experiments with similar wave conditions.
3. The flux Richardson number maintains a critical value of $\simeq \frac{1}{4}$ for $Re_\Delta < 550$ and the mud layer likely becomes supersaturated for larger Re_Δ values where stratification is intensified.
4. The threshold conditions that differentiate between the low and high Re_Δ regimes appear to result from washout of ripples and the increase in fine sand concentration in the mud layer. The latter results in an increase in settling flux and stratification in the high-concentration sediment layer, which may further contribute to the reduction in the layer thickness. However, other variables that contribute to sediment availability not tested in this study are also likely to be important, such as the degree of bed consolidation.

Acknowledgments
We would like to thank Chris Chickadel, Jim Riley, JPaul Rinehimer, Charles Nittrouer, and Andrea Ogston for support and helpful discussions, Peter Rusello and Judah Goldberg from Nortek for their technical support, and Jeffrey Parsons for initiating the work more than a decade ago and for his support during the project. This research was funded by the National Science Foundation (OCE-000488762). Data from this paper are available upon request. Please contact Alexander Horner-Devine (arhd@uw.edu).

References

Baas, J. H., J. L. Best, J. Peakall, and M. Wang (2009), A phase diagram for turbulent, transitional, and laminar clay suspension flows, *J. Sediment. Res.*, *79*(4), 162–183, doi:10.2110/jsr.2009.025.

Cacchione, D., D. Drake, and R. Kayen (1995), Measurements in the bottom boundary layer on the Amazon subaqueous delta, *Mar. Geol.*, *125*(3–4), 235–257, doi:10.1016/0025-3227(95)00014-P.

Colney, D. C., S. Falchetti, I. P. Lohmann, and M. Brocchini (2008), The effects of flow stratification by non-cohesive sediment on transport in high-energy wave-driven flows, *J. Fluid Mech.*, *610*, 43–67, doi:10.1017/S0022112008002565.

Doering, J., and A. J. Baryla (2002), An investigation of the velocity field under regular and irregular waves over a sand beach, *Coastal Eng.*, *44*(4), 275–300, doi:10.1016/S0378-3839(01)00037-0.

Downing, J. (2006), Twenty-five years with OBS sensors: The good, the bad, and the ugly, *Cont. Shelf Res.*, *26*(17–18), 2299–2318, doi:10.1016/j.csr.2006.07.018.

Falcini, F., S. Fagherazzi, and D. Jerolmack (2012), Wave-supported sediment gravity flows currents: Effects of fluid-induced pressure gradients and flow width spreading, *Cont. Shelf Res.*, *33*, 37–50, doi:10.1016/j.csr.2011.11.004.

Geyer, W. R., P. Hill, T. Milligan, and P. Traykovski (2000), The structure of the Eel River plume during floods, *Cont. Shelf Res.*, *20*, 2067–2093, doi:10.1016/S0278-4343(00)00063-7.

Goring, D., and V. Nikora (2002), Despiking acoustic Doppler velocimeter data, *J. Hydraul. Eng.*, *128*, 117–126, doi:10.1061/(ASCE)0733-9429(2002).

Grant, W. D., and O. S. Madsen (1982), Movable bed roughness in unsteady oscillatory flow, *J. Geophys. Res.*, *87*(C1), 469–481, doi:10.1029/JC087iC01p00469.

Grant, W. D., and O. Madsen (1986), The continental-shelf bottom boundary layer, *Annu. Rev. Fluid Mech.*, *18*, 265–305, doi:10.1146/annurev.fl.18.010186.001405.

Hale, R., A. S. Ogston, J. Walsh, and A. R. Orpin (2014), Sediment transport and event deposition on the Waipaoa River Shelf, New Zealand, *Cont. Shelf Res.*, *86*, 52–65, doi:10.1016/j.csr.2014.01.009.

Hamblin, A. P., and R. G. Walker (1979), Storm-dominated shallow marine deposits: The Fernie-Kootenay (Jurassic) transition, southern Rocky Mountains, *Can. J. Earth Sci.*, *16*(9), 1673–1690, doi:10.1139/e79-156.

Hanes, D. M., V. Alymov, and Y. S. Chang (2001), Wave-formed sand ripples at Duck, North Carolina, *J. Geophys. Res.*, *106*(C10), 22,575–22,592, doi:10.1029/2000JC000337.

Hare, J., A. Hay, L. Zedel, and R. Cheel (2014), Observations of the spacetime structure of flow, turbulence, and stress over orbitalscale ripples, *J. Geophys. Res. Oceans*, *119*, 1876–1898, doi:10.1002/2013JC009370.

Hay, A. E., L. Zedel, R. Cheel, and J. Dillon (2012a), Observations of the vertical structure of turbulent oscillatory boundary layers above fixed roughness using a prototype wideband coherent Doppler profiler: 2. Turbulence and stress, *J. Geophys. Res.*, *117*, C03006, doi:10.1029/2011JC007114.

Hay, A. E., L. Zedel, R. Cheel, and J. Dillon (2012b), On the vertical and temporal structure of flow and stress within the turbulent oscillatory boundary layer above evolving sand ripples, *Cont. Shelf Res.*, *46*, 31–49, doi:10.1016/j.csr.2012.02.009.

Hsu, T., and C.-D. Jan (1998), Calibration of Businger-Arya type of eddy viscosity model's parameters, *J. Waterw. Port Coastal Ocean Eng.*, *124*(5), 281–284.

Hsu, T.-J., C. E. Ozdemir, and P. A. Traykovski (2009), High-resolution numerical modeling of wave-supported gravity-driven mudflows, *J. Geophys. Res.*, *114*, C05014, doi:10.1029/2008JC005006.

Hurther, D., and U. Lemmin (2001), A correction method for turbulence measurements with a 3D acoustic Doppler velocity profiler, *J. Atmos. Oceanic Technol.*, *18*(3), 446–458.

Jaramillo, S., A. Sheremet, M. A. Allison, A. H. Reed, and K. T. Holland (2009), Wave-mud interactions over the muddy Atchafalaya subaqueous clinoform, Louisiana, United States: Wave-supported sediment transport, *J. Geophys. Res.*, *114*, C04002, doi:10.1029/2008JC004821.

Kineke, G., K. Woolfe, S. Kuehl, J. Milliman, T. Dellapenna, and R. Purdon (2000), Sediment export from the Sepik River, Papua New Guinea: Evidence for a divergent sediment plume, *Cont. Shelf Res.*, *20*(16), 2239–2266, doi:10.1016/S0278-4343(00)00069-8.

Lamb, M. P., and J. D. Parsons (2005), High-density suspensions formed under waves, *J. Sediment. Res.*, *75*(3), 386–397, doi:10.2110/jsr.2005.030.

Lamb, M. P., E. D. Asaro, and J. D. Parons (2004), Turbulent structure of high-density suspensions formed under waves, *J. Geophys. Res.*, *109*, C12026, doi:10.1029/2004JC002355.

Liang, H., M. P. Lamb, and J. D. Parsons (2007), Formation of a sandy near-bed transport layer from a fine-grained bed under oscillatory flow, *J. Geophys. Res.*, *112*, C02008, doi:10.1029/2006JC003635.

Ma, Y., L. D. Wright, and C. T. Friedrichs (2008), Observations of sediment transport on the continental shelf off the mouth of the Waiapu River, New Zealand: Evidence for current-supported gravity flows, *Cont. Shelf Res.*, *28*(4–5), 516–532, doi:10.1016/j.csr.2007.11.001.

McPhee-Shaw, E. E., D. A. Siegel, L. Washburn, M. A. Brzezinski, J. L. Jones, A. Leydecker, and J. Melack (2007), Mechanisms for nutrient delivery to the inner shelf: Observations from the Santa Barbara Channel, *Limnol. Oceanogr.*, *52*(5), 1748–1766, doi:10.4319/lo.2007.52.5.1748.

Milliman, J., and R. Meade (1983), World-wide delivery of river sediment to the oceans, *J. Geol.*, *91*(1), 1–21.

Mori, N., M. Asce, T. Suzuki, and S. Kakuno (2007), Noise of acoustic Doppler velocimeter data in bubbly flows, *J. Eng. Mech.*, *133*(1), 122–125.

Nielsen, P. (1981), Dynamics and geometry of wave-generated ripples, *J. Geophys. Res.*, *86*(C7), 6467–6472.

Nielsen, P. (1992), Coastal bottom boundary layers and sediment transport, *Adv. Ser. Ocean Eng.*, World Scientific, Singapore, River Edge, N. J. [Available at http://trove.nla.gov.au/work/20017061?selectedversion=NBD9311281.]

Nittrouer, C. A. (1999), STRATAFORM: Overview of its design and synthesis of its results, *Mar. Geol.*, *154*(1–4), 3–12, doi:10.1016/S0025-3227(98)00128-5.

Nittrouer, C. A., and L. D. Wright (1994), Transport of particles across continental shelves, *Rev. Geophys.*, *32*(1), 85–113, doi:10.1029/93RG02603.

O'Donoghue, T., J. Doucette, J. van der Werf, and J. Ribberink (2006), The dimensions of sand ripples in full-scale oscillatory flows, *Coastal Eng.*, *53*(12), 997–1012, doi:10.1016/j.coastaleng.2006.06.008.

Ogston, A., and R. Sternberg (1999), Sediment-transport events on the northern California continental shelf, *Mar. Geol.*, *154*(1–4), 69–82, doi:10.1016/S0025-3227(98)00104-2.

Ogston, A., D. Cacchione, R. Sternberg, and G. Kineke (2000), Observations of storm and river flood-driven sediment transport on the northern California continental shelf, *Cont. Shelf Res.*, *20*(16), 2141–2162, doi:10.1016/S0278-4343(00)00065-0.
Ozdemir, C. E., T.-J. Hsu, and S. Balachandar (2010a), A numerical investigation of fine particle laden flow in an oscillatory channel: The role of particle-induced density stratification, *J. Fluid Mech.*, *665*, 1–45, doi:10.1017/S0022112010003769.
Ozdemir, C. E., T.-J. Hsu, and S. Balachandar (2010b), Simulation of fine sediment transport in oscillatory boundary layer, *J. Hydro-environ. Res.*, *3*(4), 247–259, doi:10.1016/j.jher.2009.10.013.
Ozdemir, C. E., T.-J. Hsu, and S. Balachandar (2011), A numerical investigation of lutocline dynamics and saturation of fine sediment in the oscillatory boundary layer, *J. Geophys. Res.*, *116*, C09012, doi:10.1029/2011JC007185.
Ozdemir, C. E., T.-J. Hsu, and S. Balachandar (2014), Direct numerical simulations of transition and turbulence in smooth-walled Stokes boundary layer, *Phys. Fluids*, *26*(4), 045108, doi:10.1063/1.4871020.
Parsons, J., J. Bush, and J. Syvitski (2001), Hyperpycnal plume formation from riverine outflows with small sediment concentrations, *Sedimentology*, *48*(2), 465–478, doi:10.1046/j.1365-3091.2001.00384.x.
Puig, P., A. Ogston, B. Mullenbach, C. Nittrouer, and R. Sternberg (2003), Shelf-to-canyon sediment-transport processes on the Eel continental margin (northern California), *Mar. Geol.*, *193*(1–2), 129–149, doi:10.1016/S0025-3227(02)00641-2.
Roberts, J., and R. Jepsen (1998), Effects of particle size and bulk density on erosion of quartz particles, *J. Hydraul. Eng.*, *124*(12), 1261–1267.
Safak, I., M. Allison, and A. Sheremet (2013), Floc variability under changing turbulent stresses and sediment availability on a wave energetic muddy shelf, *Cont. Shelf Res.*, *53*, 1–10, doi:10.1016/j.csr.2012.11.015.
Scully, M., C. Friedrichs, and L. Wright (2002), Application of an analytical model of critically stratified gravity-driven sediment transport and deposition to observations from the Eel River continental shelf, Northern California, *Cont. Shelf Res.*, *22*(14), 1951–1974, doi:10.1016/S0278-4343(02)00047-X.
Sternberg, R., and D. Cacchione (1996), Observations of sediment transport on the Amazon subaqueous delta, *Cont. Shelf Res.*, *16*(5), 697–715, doi:10.1016/0278-4343(95)00045-3.
Thorne, P., J. Williams, and A. Davies (2002), Suspended sediments under waves measured in a large-scale flume facility, *J. Geophys. Res.*, *107*(C8), doi:10.1029/2001JC000988.
Thorne, P. D., A. G. Davies, and P. S. Bell (2009), Observations and analysis of sediment diffusivity profiles over sandy rippled beds under waves, *J. Geophys. Res.*, *114*, C02023, doi:10.1029/2008JC004944.
Traykovski, P., W. Geyer, J. Irish, and J. Lynch (2000), The role of wave-induced density-driven fluid mud flows for cross-shelf transport on the Eel River continental shelf, *Cont. Shelf Res.*, *20*(16), 2113–2140, doi:10.1016/S0278-4343(00)00071-6.
Traykovski, P., P. Wiberg, and W. Geyer (2007), Observations and modeling of wave-supported sediment gravity flows on the Po prodelta and comparison to prior observations from the Eel shelf, *Cont. Shelf Res.*, *27*(3–4), 375–399, doi:10.1016/j.csr.2005.07.008.
Traykovski, P., J. Trowbridge, and G. Kineke (2015), Mechanisms of surface wave energy dissipation over a high-concentration sediment suspension, *J. Geophys. Res. Oceans*, *120*, 1638–1681, doi:10.1002/2014JC010245.
Trowbridge, J. H., and G. C. Kineke (1994), Structure and dynamics of fluid muds on the Amazon, *J. Geophys. Res.*, *99*(C1), 865–874, doi:10.1029/93JC02860.
Turner, J. (1973), *Buoyancy Effects in Fluids*, 368 p., Cambridge Univ. Press, N. Y.
Van Rijn, L. (1993), *Principles of Sediment Transport in Rivers, Estuaries and Coastal Seas*, Aqua Publ., Amsterdam, Netherlands.
Van Rijn, L. (2007), Unified view of sediment transport by currents and waves. II: Suspended transport, *J. Hydraul. Eng.*, *133*(6), 668–689.
Vongvisessomjai, S. (1984), Oscillatory ripple geometry, *J. Hydraul. Eng.*, *110*(3), 247–266, doi:10.1061/(ASCE)0733-9429(1984)110:3(247).
Walsh, J., C. Nittrouer, C. Palinkas, A. S. Ogston, R. Sternberg, and G. Brunskill (2004), Clinoform mechanics in the Gulf of Papua, New Guinea, *Cont. Shelf Res.*, *24*(19), 2487–2510, doi:10.1016/j.csr.2004.07.019.
Wheatcroft, R. A., A. W. Stevens, and R. V. Johnson (2007), In situ time-series measurements of subseafloor sediment properties, *IEEE J. Oceanic Eng.*, *32*(4), 862–871, doi:10.1109/JOE.2007.907927.
Wiberg, P., and J. D. Smith (1983), A comparison of field data and theoretical models for wave-current interactions at the bed on the continental shelf, *Cont. Shelf Res.*, *2*(2–3), 147–162, doi:10.1016/0278-4343(83)90013-4.
Wiberg, P. L., and C. K. Harris (1994), Ripple geometry in wave-dominated environments, *J. Geophys. Res.*, *99*(C1), 775–789, doi:10.1029/93JC02726.
Winterwerp, J. C. (2006), Stratification effects by fine suspended sediment at low, medium, and very high concentrations, *J. Geophys. Res.*, *111*, C05012, doi:10.1029/2005JC003019.
Wright, L., and C. Friedrichs (2006), Gravity-driven sediment transport on continental shelves: A status report, *Cont. Shelf Res.*, *26*(17–18), 2092–2107, doi:10.1016/j.csr.2006.07.008.
Wright, L., C. Sherwood, and R. Sternberg (1997), Field measurements of fairweather bottom boundary layer processes and sediment suspension on the Louisiana inner continental shelf, *Mar. Geol.*, *140*(3), 329–345, doi:10.1016/S0025-3227(97)00032-7.
Wright, L., S.-C. Kim, and C. Friedrichs (1999), Across-shelf variations in bed roughness, bed stress and sediment suspension on the northern California shelf, *Mar. Geol.*, *154*(1–4), 99–115, doi:10.1016/S0025-3227(98)00106-6.
Wright, L., C. Friedrichs, S. Kim, and M. Scully (2001), Effects of ambient currents and waves on gravity-driven sediment transport on continental shelves, *Mar. Geol.*, *175*(1–4), 25–45, doi:10.1016/S0025-3227(01)00140-2.
Yan, B., Q. Zhang, and M. Lamb (2010), Time-averaged turbulent mixing and vertical concentration distribution of high-density suspensions formed under waves, *Coastal Eng.*, *32*, 1–8.